JPhys Energy

PAPER • OPEN ACCESS

Optimization of Sb_2Se_3 thin-film solar cells: the role of absorber selenization and the CdS buffer layer

To cite this article: David Payno *et al* 2026 *J. Phys. Energy* **8** 015020

Journal of Physics: Energy

OPEN ACCESS

RECEIVED
9 October 2025

REVISED
14 January 2026

ACCEPTED FOR PUBLICATION
26 January 2026

PUBLISHED
6 February 2026

PAPER

Optimization of Sb_2Se_3 thin-film solar cells: the role of absorber selenization and the CdS buffer layer

David Payno[1,2], Yudania Sánchez[3], Marin Rusu[4], Luna Lázaro-Castrillón[1], Samira Khelifi[5], Beatriz Galiana[6], Víctor Bonal[2], Sanja Djurdjić Mijin[2,7], Antonio Arranz[2], Mati Danilson[8], Snežana Lazić[2], Maarja Grossberg-Kuusk[8], Thomas Unold[4], Rosalia Serna[1], José Manuel Merino[2] and Raquel Caballero[1,*]

[1] Instituto de Óptica Daza de Valdés-CSIC, Calle Serrano 121, 28006 Madrid, Spain
[2] Universidad Autónoma de Madrid, Calle Francisco Tomás y Valiente 7, 28049 Madrid, Spain
[3] IREC, Catalonia Institute for Energy Research, C/ Jardins de les Dones de Negre 1, Barcelona 08930, Spain
[4] Department Structure and Dynamics of Energy Materials, Helmholtz-Zentrum Berlin für Materialien und Energie, Lise-Meitner Campus, Hahn-Meitner-Platz 1, 14109 Berlin, Germany
[5] Ghent University, Department of Solid-State Sciences, Krijgslaan 281, 9000 Gent, Belgium
[6] Universidad Carlos III de Madrid, Avda. Universidad 40, 28911 Leganés, Madrid, Spain
[7] Institute of Physics Belgrade, University of Belgrade, Pregrevica 1118, 11080 Belgrade, Serbia
[8] Department of Materials and Environmental Technology, Tallinn University of Technology, Ehitajate tee 5, 19086 Tallinn, Estonia
[*] Author to whom any correspondence should be addressed.

E-mail: raquel.caballero@csic.es

Keywords: Sb_2Se_3, CdS, selenization, substrate solar cells

Supplementary material for this article is available online

Abstract

Sb_2Se_3 has garnered significant interest as a potential material for photovoltaic (PV) devices, owing to its unique properties. Here, Sb_2Se_3 thin films are grown by selenization of evaporated Sb layers. The Se content and maximum temperature during the selenization process control the composition of the semiconductor. In all cases, the Sb_2Se_3 is orientated in the [hk1] direction. The increase of Se temperature results in larger grain size; however, the process temperature must be limited to 340 °C to avoid a significant excess of Se and the formation of holes on the Sb_2Se_3 surface, which leads to decreased performance of the ITO/ZnO/CdS/Sb_2Se_3/Mo/SLG device. As determined by surface photovoltage, combined Kelvin probe and photoelectron yield spectroscopy measurements, Sb_2Se_3 thin films exhibit p-type conductivity with a doping concentration of approximately 4×10^{15} cm^{-3}. Two different buffer layers, CdS1 and CdS2, are studied to form the heterojunction. The use of Na citrate as chemical reagent, along with modified chemical bath conditions for CdS2 deposition, results in enhanced PV performance, increasing the device efficiency from 3.6% to 5.4%. This improvement may be related to the superior optical properties of the CdS2 with higher bandgap energy and lower total reflectance, allowing for a higher carrier collection. The observed Cd diffusion towards the active layer, likely results in the formation of Cd_i donors that contribute to a stronger downward band bending at the buffer/absorber interface, reducing interface recombination and enhancing open circuit voltage of the devices. Although the modification of the CdS layer plays a key role in improving the device performance, the efficiency of fabricated devices remains limited by interface recombination. A total area efficiency of 5.5% is achieved by reducing the thickness of Sb_2Se_3 to 450 nm. This study demonstrates the relevance of optimizing the CdS/Sb_2Se_3 heterointerface to produce efficient Sb_2Se_3 PV devices.

1. Introduction

Low-dimensional antimony-chalcogenide materials have received an outstanding interest for photovoltaic (PV) devices in recent years. They show unique properties as absorbers for thin-film solar energy harvesting [1], including high stability, low environmental impact, low cost, low carbon footprint and

Table 1. Selenization parameters used to form Sb_2Se_3 thin films.

Sample	Se (mg)	T_{Se} (°C)	t (min)	Thickness (nm)
1_15 1_22 1_30	15 22 30	320	30	400 450 450
2_320 2_340 2_360	25 25 25	320 340 360	60 60 60	1200 1300 1300
3_340	25	340	60	1000
4_340	25	340	60	1300
5_340	25	340	60	450

high technological flexibility. In particular, Sb_2Se_3 shows a high absorption coefficient $> 10^5$ cm^{-1}, p-type conductivity under Se-rich conditions, high stability and a much lower melting point than that of Cu(In, Ga)Se_2 (CIGS), CdTe and $Cu_2ZnSn(S, Se)_4$ (CZTSSe), enabling lower processing temperatures. This material exhibits a quasi-one-dimensional crystal structure, with grain boundaries that are inherently benign to charge-carrier recombination. In addition, Sb_2Se_3 has a completely different coordination environment compared with tetrahedrally coordinated CIGS and CZTSSe, meaning that one of the main limitations of those materials—the cation disorder introducing severe band tails and strong recombination pathways—is absent in Sb chalcogenides.

Nowadays, both superstrate and substrate Sb_2Se_3-based solar cells have already achieved efficiencies above 10% [2]. Different deposition techniques have been used to control the Sb_2Se_3 film orientation, a key factor to achieve high efficiency solar cells due to the anisotropic physical properties, ranging from chemical to physical routes [2–5]. The film orientation together with the complex bulk defects limit the PV device performance, well below the theoretical value [6]. Another crucial factor for enhancing device performance is the optimization of the *p–n* heterojunction to ensure efficient charge carriers transport. This is particularly important, not only in the superstrate configuration [7], but also in the substrate configuration. Currently, different laboratories are exploring various electron transport layers for Sb_2Se_3 thin film solar cells as TiO_2 [8], ZnSnO [9], SnO_2 [10] and CdS [4]. CdS is the standard buffer layer used in different thin-film solar cell technologies including CIGS, CZTSSe and Sb_2Se_3 based devices. However, the non-optimal band alignment between Sb_2Se_3 and CdS, has motivated several studies to incorporate dopants into the buffer layer, therefore controlling the doping carrier density and tuning the heterojunction band alignment [7, 11, 12].

In this study, Sb_2Se_3 thin films were grown by the selenization of evaporated Sb layer onto Mo/SLG substrates. In order to optimize the absorber layer, we investigate first different growth parameters, including the thickness of the Sb precursor layer, selenization temperature and amount of elemental Se added during the thermal treatment. In addition, we study the influence of the CdS buffer layer on the substrate PV device configuration (ITO/ZnO/CdS/ Sb_2Se_3/Mo/SLG). For that, two completely different CdS chemical bath recipes were used, demonstrating the importance of the optimization of the buffer layer to enhance the solar cell efficiency.

2. Experimental method

Sb_2Se_3 thin films fabrication. Sb_2Se_3 thin films were grown by selenization of thermally evaporated Sb layers at room substrate temperature [13]. The base pressure in the vacuum chamber was $\sim 10^{-7}$ mbar, while the working pressure was in the range of 10^{-6} mbar. The evaporation rate of the Sb layers was around 1 Å s^{-1}. Sb layers with different thicknesses were deposited onto Mo/SLG back contact. The thickness of the Sb layers was controlled by adjusting the evaporation time. Subsequently the Sb precursor layers were placed into a quasi-closed graphite box inside a tubular furnace and selenized at atmospheric pressure under Ar atmosphere. Different amounts of elemental Se were added, 15, 22, 25 and 30 mg Se, as well as different selenization temperatures, 320 °C, 340 °C, 360 °C, 380 °C and 400 °C, were used during the selenization process. The furnace was naturally cooled down to room temperature once the selenization process was finished. Table 1 summarizes the selenization parameters used to form Sb_2Se_3 films. Sb_2Se_3 thin films with the same Series number were fabricated from the same Sb precursor layer, ensuring identical starting conditions. The only distinction among the samples lies in the variation of one the selenization process parameters (Se content or temperature), as shown in table 1. Specifically, Series 1 investigates the influence of the amount of Se added during selenization, Series 2 examines the effect of the selenization temperature, and Series 3, 4, and 5 apply the same selenization parameters but differ in the thickness of the Sb_2Se_3 absorber layer.

Table 2. Chemical conditions for CdS thin film growth using a chemical bath deposition (CBD) process.

Sample	Cd precursor (M)	Chemical reagents (M)	pH
CdS1	$CdSO_4$ (0.1 M)	NH_4Cl (0.5 M) CH_4N_2S (0.3 M) NH_4OH (1.6 M)	10.5
CdS2	$Cd(NO_3)_2$ (0.01 M)	$Na_3H_2(C_3H_5O(COO)_3)$ (0.1 M) Thiourea (CH_4N_2S) (0.1 M) NH_4OH (28%–30% w/w)	10

Device fabrication: Two different chemical bath deposition (CBD) routes, CdS1 and CdS2, were compared for the growth of CdS thin films. The first recipe, CdS1, used $CdSO_4$ (0.1 M) as cadmium precursor, NH_4Cl (0.5 M) as a weak complexing agent, a relatively high thiourea concentration (0.3 M), and NH_4OH (1.6 M). Under these conditions, the bath pH was adjusted to 10.5, favoring a rapid S^{2-} release and fast CdS precipitation. In contrast, CdS2 was prepared using $Cd(NO_3)_2$ (0.01 M) as cadmium precursor, sodium citrate (0.1 M) as an effective chelating agent providing stronger Cd^{2+} stabilization compared to NH_4Cl, and a lower thiourea concentration (0.1 M). Concentrated NH_4OH (28%–30% w/w) was added until reaching a stable bath pH of 10. These conditions slow down the S^{2-} release and stabilize Cd^{2+} in solution, resulting in a more controlled film growth (see table 2). These variations in CdS buffer layer deposition are based on previous investigations carried out on kesterite thin-film solar cells, as reported in [14]. A window layer composed of i-ZnO (50 nm) and In_2O_3:SnO_2 (ITO) (200 nm) layers was deposited by RF-pulsed sputtering deposition. Neither grids nor an anti-reflection coating were deposited onto the final PV devices. Moreover, no thermal treatment was applied to the solar cells [15].

Characterization: x-ray Fluorescence (XRF) measurements were carried out to analyze the elemental composition of Sb_2Se_3 thin films using a calibrated Fischerscope x-ray XDAL 237 system. Grazing incidence x-ray diffraction (GIXRD) was performed to study the structural properties of the chalcogenide thin films and to identify the different phases. GIXRD data were collected with a PANAlytical X´Pert Pro MPD diffractometer, using CuK_α radiation and a multilayer mirror to produce a parallel beam. Detector scans with incident angle of 4° were carried out [15]. The morphology of the Sb_2Se_3/Mo/glass structure was analyzed by scanning electron microscopy (SEM) using a FEI VERIOS 460, operating at 2 kV. Cross-sectional specimens suitable for high-resolution transmission electron microscopy (HRTEM) characterization were prepared using a focused ion beam Helios 600 dual-beam system and examined in a Talos F200X field emission TEM/STEM operating at 200 keV with four symmetrical EDX detectors. Raman scattering measurements of the chalcogenide layers were carried out using a Horiba Jobin Yvon T64000 triple-monochromator Raman system with the 1800/1800/1800 grooves/mm in backscattering micro-Raman configuration. The 514.5 nm emission line of a mixed Ar+/Kr+ gas laser was used as an excitation source. The laser beam was focused using an Olympus objective with 0.8 NA and 50x magnification. The laser power was limited to a maximum of 0.6 mW, and the laser spot size was approximately 5 μm. The spectral calibration was performed by using the main phonon peak at 520 cm^{-1} of a bulk monocrystalline Si wafer as a reference. Measurements were performed at room temperature in ambient air in both parallel and crossed polarization configurations, with a data acquisition time of 15 min and 10 accumulations per spectrum. Fourier Transform infrared (FTIR) measurements were performed using a Bruker Vertex 80 V spectrometer. The data were recorded in reflectance mode and then converted into absorbance spectra using Kubelka–Munk function. X-ray photoelectron spectroscopy (XPS) analysis was performed in an ultra-high vacuum system using a hemispherical analyzer (SPECS Phoibos 100 MCD-5) and non-monochromatized Mg Kα (1253.6 eV) radiation from a twin anode (Al–Mg) x-ray source at a constant power of 300 W. The pass energy was 9 eV, providing a constant resolution of 0.9 eV. The observed sample charging was corrected by referencing the C 1s peak of C–C species at 285.0 eV and shifting accordingly all other core levels. The satellites peaks from the non-monochromatic x-ray source were removed from the spectra using CasaXPS software [16]. Total and straight-through transmittance, and, total and diffuse reflectance measurements were performed for the CdS buffer layers with a Cary Varian 5000 spectrophotometer in a range from 300 to 1500 nm. The total transmittance and reflectance were measured using an integrating sphere. Kelvin probe (KP) and Photoelectron Yield Spectroscopy (PYS) measurements were carried out at ambient pressure under an inert nitrogen (N_2) atmosphere at room temperature by a KP Technology SKP5050-APS02 instrument [17, 18]. The controlled illumination of the sample and shielding from external electric fields was achieved by placing the setup in a Faraday cage. The samples were contacted with conductive carbon

tape. The top counter electrode was a 2.0 mm-diameter gold-alloy-coated electrode. KP measurements were performed with the vibrating top reference (Kelvin) probe, with a work function, Φ_{tip}, calibrated against a gold reference sample. The work function of the sample, Φ_{sample}, was determined according to the relation $\Phi_{sample} = \Phi_{tip} + e{\cdot}CPD$, where e is the elementary charge and CPD is the contact potential difference between the KP tip and the studied sample. The CPD was measured with a resolution of 1–3 mV. The surface photovoltage (SPV), defined as $SPV = CPD_{light} - CPD_{dark}$ was measured using laser diodes with wavelengths/energies of 405 nm/3.06 eV and 670 nm/1.85 eV, as well as a white light source with spectral distribution corresponding to a color temperature of 5700 K. The incident power density of all the light sources was adjusted to approximately100 Mw cm^{-2}. As noted, the SPV can also be expressed as $SPV = \Phi_{light} - \Phi_{dark}$. The sign of the SPV indicates the type of charge carriers that accumulate at the surface adjacent to the Kelvin tip. Under illumination, electrons separate toward the surface of a *p*-type material due to its typical downward band bending, which arises from different surface terminations and defects. In the case of downward band bending, one obtains $\Phi_{light} > \Phi_{dark}$ and thus an $SPV > 0$, which is characteristic of a *p*-type conductive material (see the band diagrams in the supporting information of [17] for more details). On the contrary, an $SPV < 0$ indicates hole accumulation at the material surface, corresponding to upward band bending characteristic of an *n*-type semiconductor surface. In the case of solar cells or multilayer film stacks, the SPV polarity identifies the built-in field direction and device polarity. PYS measurements were performed by using the same Kelvin tip operated in a static regime at a tip-sample distance of less than 1 mm. A bias voltage of 10 V was applied between the sample and the electrode to collect the photoexcited charge carriers. The sample was illuminated with a deuterium light source coupled to a grating monochromator, providing excitation in the photon energy range of 3.4–7.6 eV. Measurements were conducted with a wavelength step of 1 nm and the photoemission threshold was determined with a resolution of 30 meV. The light was guided through a DUV optical fiber and focused onto the sample as an elliptical spot of approximately 2×3 mm^2. Further details on the KP-PYS setup and data evaluation procedures can be found elsewhere [17].

Current–Voltage (*I–V*) characteristics of the PV devices were measured by using a Sun 3000 class solar simulator (Abet Technologies Inc., Milford, Connecticut, USA) under standard test conditions (25 °C, AM 1.5, 100 mW cm^{-2}). External quantum efficiency (EQE) of the solar cells was measured using a Bentham PVE300 system (Bentham Instruments Ltd, Berkshire, UK) calibrated with a Si and Ge photodiodes [13, 15]. Capacitance voltage (*C–V*) and drive-level capacitance profiling (DLCP) were performed using a HP 4192 A LF impedance analyzer (5 Hz–13 MHz) at a frequency $f = 100$ kHz.

3. Results and discussion

3.1. Sb_2Se_3 thin films

In the Series 1, the Sb layer had a thickness of only 200 nm, yielding a final thickness of approximately 400 nm after selenization when 15 mg of Se was added, and around 450 nm when 22 mg or 30 mg of Se was incorporated. (See table 1). The addition of 22 mg and 30 mg of Se led to the same composition, with a [Sb]/[Se] atomic ratio of 0.54, while the reduction of Se to 15 mg decreased the incorporation of Se into the Sb_2Se_3 lattice resulting in a [Sb]/[Se] atomic ratio of 0.61, as determined by XRF. Thus, the incorporated Se is saturated once 22 mg Se is added during the selenization process. In all cases, the samples were Se-rich. Se-rich conditions help to prevent the formation of undesirable donor-like defects such as Se vacancy, V_{Se} [19], which reduce the *p*-type conductivity and are detrimental to device performance. As reported by Kim *et al* [20], it is crucial to control the Se flux during deposition because the chalcogen concentration determines the population of V_{Se} defects and can modify the preferred orientation.

The structural properties of the Sb_2Se_3 thin films from Series 1 were further analyzed by XRD. Figure 1(a) presents the XRD patterns measured using a grazing incidence angle of 4°. All the thin films exhibit an orthorhombic crystal structure (JCPDS – 00-015-0861). Mo diffraction peaks are also detected and the formation of $MoSe_2$ phase cannot be ruled out. The texture coefficients (TCs) of the main (hk0) and (hk1) planes, within the 2θ range of 10°–60°, of the three Sb_2Se_3 absorber layers were calculated (see figure 1(b)). The TC is defined as follows:

$$TC = \frac{I_{(hkl)}/I_{0(hkl)}}{1/N\left[\sum_{i=1}^{N} I(h_i k_i l_i)/I_0(h_i k_i l_i)\right]} \quad (1)$$

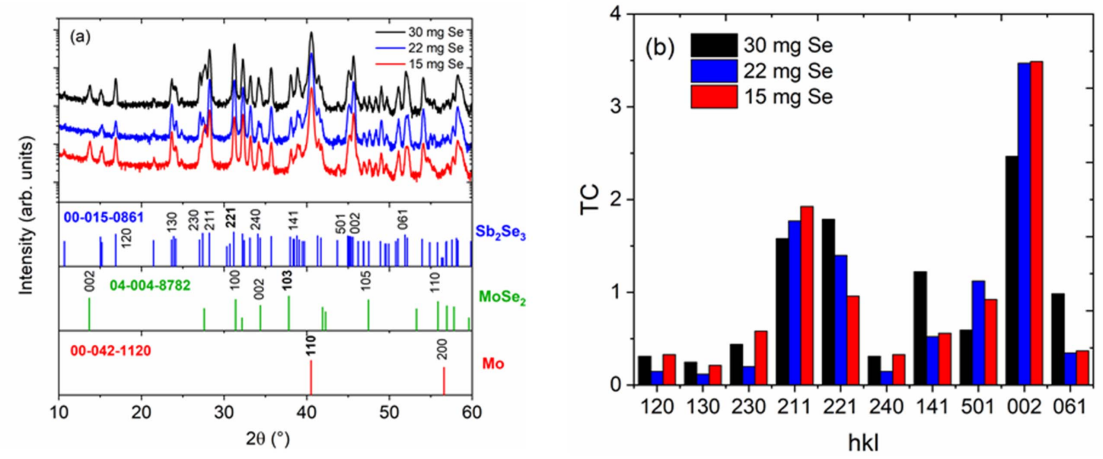

Figure 1. (a) XRD pattern using grazing incidence angle of 4° and (b) XRD texture coefficient (TC) of Sb_2Se_3 thin films grown using different amounts of Se added during the selenization process (Series 1).

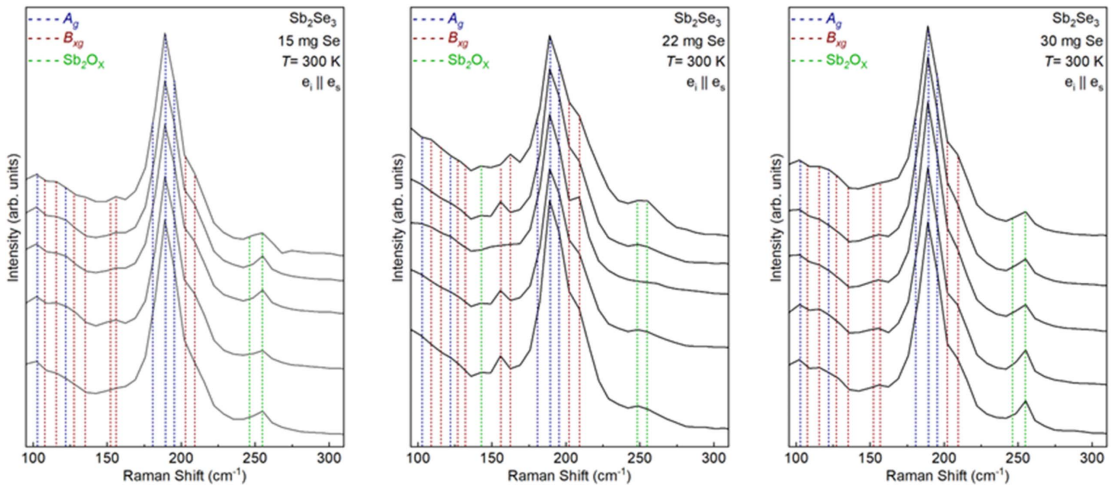

Figure 2. Raman spectra of samples of Series 1 with different amount of Se added during the selenization process. Blue and red vertical lines were added to indicate the A_g and B_{xg} characteristic modes of pure Sb_2Se_3 respectively, and, purple to indicate the Sb oxide vibrational modes.

where $I(hkl)$ is the measured intensity of the diffraction peak, $I_0(hkl)$ is the relative intensity value obtained from the JCPDS # 00-015-0861, and N is the total number of considered reflections. In general, a TC value greater than 1 for a given (hkl) plane indicates that the film has a (hkl) preferential orientation. As shown in figure 1(b), the calculated TC of the Sb_2Se_3 (002) diffraction peak increases to maximum values of 3.49 and 3.47 for samples selenized with 15 mg and 22 mg of Se, respectively, but decreases to 2.47 upon increasing the Se amount to 30 mg. However, this trend does not reflect a weakening of the overall $[hk1]$ orientation when increasing Se content. When considering all ten diffraction peaks included in this study, as shown in figure S1 of the supplementary information, the average [hk1] TCs are 1.37, 1.44, and 1.44 for samples selenized with 15, 22, and 30 mg Se, respectively, while the corresponding average $[hk0]$ values are 0.36, 0.15, and 0.31. Thus, Sb_2Se_3 thin films consistently exhibit a preferential orientation in the $[hk1]$ direction, which is beneficial for the charge carrier's transport [21].

Complementary structural information was obtained by Raman spectroscopy, as shown in figure 2. The Raman spectra host five A_g and eight B_{xg} vibrational modes characteristic of orthorhombic Sb_2Se_3, along with two additional modes above 215 cm^{-1} attributed to the formation of a superficial oxide layer. The formation of Sb_2O_3 is detrimental to device performance, serving as recombination center in Sb_2Se_3-based thin-film solar cells, as reported in [22, 23].

As reported in [11, 24], the selenization of the Sb precursor layer proceed through a sequence of stages. Initially, Se melts and transitions into vapor, which diffuses to the Sb surface and initiates the formation of Sb_2Se_3 nuclei. As the Se vapor pressure increases, Se continues to diffuse along the

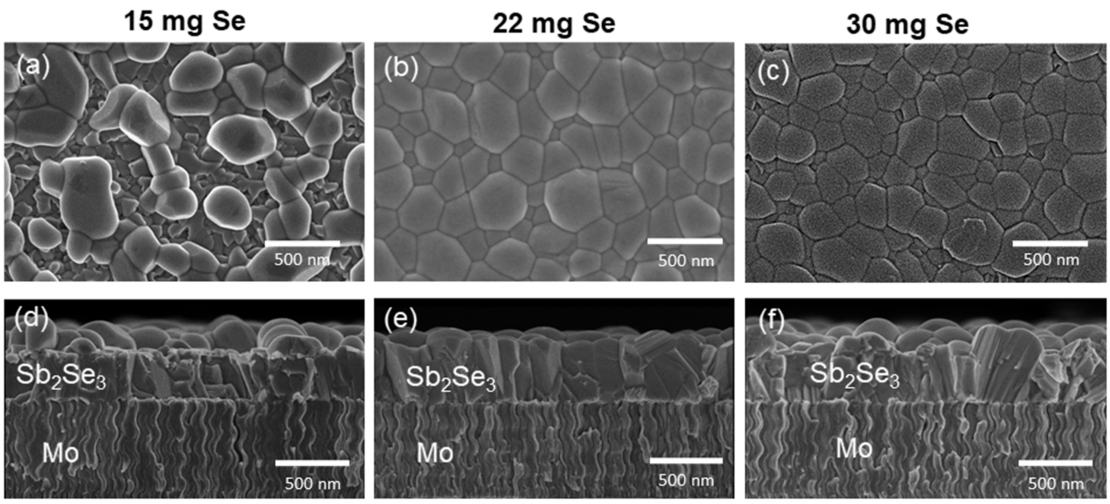

Figure 3. Surface morphology of Sb_2Se_3 thin films and cross-sectional SEM images of Sb_2Se_3/Mo structures fabricated by adding (a), (d) 15 mg Se (Sample 1_15), (b), (e) 22 mg Se (Sample 1_22) and (c), (f) 30 mg Se (Sample 1_30) during the selenization process, performed at 320 °C for 30 min, using 200 nm-thick Sb precursor layer.

$(Sb_2Se_6)_n$ gaps within the film, reacting progressively with the underlying Sb precursor converting it fully into Sb_2Se_3. This is followed by a crystallization process stage in which the Sb_2Se_3 grain grow until the selenization process ends. In the present work, a similar behavior occurs. Figure 3 shows the surface morphology of the Sb_2Se_3 and the cross-sectional SEM picture of the Sb_2Se_3/Mo structure. Samples 1_22 and 1_30 present a compact and uniform surface, while sample 1_15 presents a superposition of grains of different sizes with larger grains located near the surface. This prominent grain size growth at the top surface is no longer observed when 22 mg Se is added during the selenization process, and the Sb_2Se_3 grain size remains nearly constant for Se amounts exceeding 15 mg. Despite the higher [Sb]/[Se] atomic ratio of 0.61 for sample 1_15, this Se amount promotes Sb_2Se_3 crystal growth, yielding larger grains at the top surface at selenization temperature of 320 °C, however, it is insufficient to produce a uniform absorber surface. In all cases, a compact Sb_2Se_3/Mo structure is formed, free of pinholes that could create electrical shunting paths. Cross-sectional SEM images clearly reveal the vertical growth of the Sb_2Se_3 thin films, particularly for those selenized with 22 and 30 mg of Se. These films also exhibit faceted morphologies which are indicative of high crystalline quality. In contrast, the prominent surface grains are distinctly observed in the cross-sectional SEM image of Sample 1_15.

Power conversion efficiencies exceeding 10% have been reported for Sb_2Se_3 absorber layer of around 1.2–1.5 μm in thickness [3]. To further explore this regime, a second series of samples (Series 2) was prepared, consisting of Sb_2Se_3 thin films with thicknesses of approximately 1.2–1.3 μm. The influence of the selenization temperature (T_{Se}) was systematically investigated at 320 °C, 340 °C, and 360 °C, using 25 mg of Se and a dwelling time of 60 min in all cases. The dwelling time was doubled compared to Series 1 to ensure sufficient Se diffusion throughout the entire Sb layer during the selenization process. For the remaining experiments, we selected Se amounts between 22 and 30 mg for the following reasons: i) the Sb precursor layer in Series 2 was thicker compared to that in Series 1, therefore using more than 15 mg of Se ensured sufficient Se diffusion throughout the entire Sb layer and ii) this Se amount ensured Se-rich Sb_2Se_3 thin films, which is recommended to obtain p-type conductivity and to avoid the formation of Se-vacancy defects.

As shown in figure 4(a), increasing the selenization temperature results in a higher incorporation of Se, as confirmed by XRF measurements performed at eight different points on each sample, with the effect being most pronounced at 360 °C. The higher temperature enhances Se diffusion and reaction kinetics through the entire Sb precursor layer, which is incorporated in the lattice, resulting in better film crystallinity and reduced Se vacancies.

Figures 4(b)–(g) show the surface of the absorber layer grown using the different selenization temperatures and the cross-sectional SEM images of Sb_2Se_3/Mo structures.

A higher selenization temperature leads to an increase in Sb_2Se_3 grain size, as expected for a thermally activated process, with the effect becoming particularly pronounced at temperatures approaching 340 °C. In addition, a slightly thicker chalcogenide absorber layer is obtained when the selenization temperature increases. In all the cases, a dense and compact Sb_2Se_3/Mo structure free of pinholes

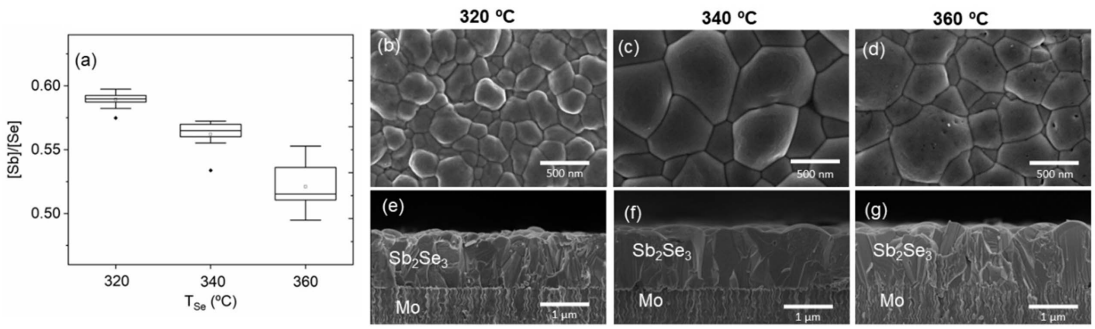

Figure 4. (a) [Sb]/[Se] atomic ratio of Sb_2Se_3 layers selenized at different temperatures. Surface morphologies of Sb_2Se_3 thin films and cross-sectional SEM images of the Sb_2Se_3/Mo structures produced by the selenization of the Sb precursor layer at selenization temperature of (b), (e) 320 °C (Sample 2_320), (c), (f) 340 °C (Sample 2_340) and (d), (g) 360 °C (Sample 2_360).

is formed. However, some small holes are detected on the surface of the Sb_2Se_3 thin film selenized at 360 °C, indicating a lower quality of this absorber structure as observed in figure 4(g).

In order to investigate and corroborate the increase in Se content with increasing selenization temperature, Sb_2Se_3 thin films were grown at 340 °C, 360 °C, 380 °C, and 400 °C for 1 h under atmospheric pressure, with the addition of 25 mg of Se. Figure S2 in the supplementary information shows the variation of the [Sb]/[Se] atomic ratio with temperature, reflecting an increase in Se content at higher temperatures, although the rate of this increase becomes less pronounced when the temperature exceeds 380 °C. SEM images of these absorber layers (see figure S2) reveal that an increase in the selenization temperature leads to the formation of large holes on the Sb_2Se_3 surface, starting at 360 °C. EDX measurements performed inside and outside the holes of the absorber selenized at 380 °C, along with EDX mapping, confirm that these holes can extend down to the Mo back contact. As mentioned above, small holes already begin to appear on the absorber surface selenized at 360 °C, as shown in figure 4(d). Controlling Se content is crucial since Se-rich conditions help to prevent the formation of undesirable V_{Se} defects. Additionally, an excess of Se-rich can result in the formation of acceptor-like Se_{Sb} defects, which has a much lower formation energy than V_{Se} and Sb_{Se} under Se-rich conditions [25]. Hybrid density functional theory reported that Se_{Sb} acts as detrimental recombination centers, occupying midgap states [26].

Nevertheless, similar to the results obtained for Series 1, all Sb_2Se_3 thin films of Series 2 exhibit a preferential orientation along the [*hk1*] direction (see figure S3 in the supplementary information). The calculated TC of the Sb_2Se_3 (002) peak is the highest for all samples; however, the relative intensities of the (*hk*0) reflections are higher at lower selenization temperature. FTIR spectroscopy measurement was conducted in the absorber 2_240, confirming the presence of Sb_2Se_3 together with a significant contribution from Sb_2O_x, which is detrimental to device performance (see figure S4 in the supplementary information).

3.2. Sb_2Se_3 thin-film solar cells

Table 3 shows the PV parameters of the best solar cells produced using the Sb_2Se_3 absorber layers described in table 1. The integrated short circuit current density J_{SC} determined from EQE measurements is presented in brackets, together with the efficiency calculated using this integrated value (efficiency in active area). In the Series 1, much thinner Sb_2Se_3 absorbers than those of Series 2, the active-area devices performance is in the range of 4% independent from the Se amount added during the selenization process. However, the solar cell fabricated with the highest Se addition presents a lower fill factor FF, which limits the overall device efficiency. Moreover, the average total-area efficiencies measured from seven devices per sample in Series 1, are 3.49%, 3.47% and 3.33% for the 1_15, 1_22 and 1_30 solar cells, respectively. Therefore, these average values show that Sample 1_30 exhibits the poorest device performance. However, the alterations in selenium content does not yield significant performance differences. Figure 5 shows the EQE measurements of these three PV devices measured at 0 V and −1 V reverse bias. The same CdS1, i-ZnO and ITO layers were used for the different solar cells. The difference between the EQE spectra measured without bias and under reverse bias reveals limited carrier collection efficiency, as the increased depletion width at—1 V enhances charge extraction [27]. This effect is particularly pronounced for Sample 1_22, which may account for its lower open circuit voltage V_{OC} and J_{SC} of that solar cell. Enhanced carrier collection is observed for the device fabricated with 15 mg of Se, achieving an active-area efficiency of 4.2%.

Table 3. PV parameters of the best Sb_2Se_3 thin-film solar cells corresponding to the absorber layers of table 1. In Series 3, influence of the CdS buffer layer variation was studied.

Device	V_{OC} [mV]	J_{SC} (mA cm^{-2})	FF [%]	η [%]	R_{sh} (Ω·cm^2)	R_s (Ω·cm^2)
1_15	368	20.2 (22.2)	51.3	3.8 (4.2)	146.6	2.7
1_22	352	19.6 (21.0)	51.9	3.6 (3.8)	220.7	1.5
1_30	381	19.8 (22.2)	48.4	3.7 (4.1)	187.1	2.5
2_320	349	16.4 (8.5)	41.7	2.4 (1.2)	138.0	4.3
2_340	381	20.1 (15.6)	50.9	3.9 (3.0)	173.0	2.6
2_360	371	25.2 (11.9)	33.3	3.1 (1.5)	32.3	6.0
3_340	370	19.8 (21.3)	46.1	3.4 (3.6)	137.8	5.6
3_340_2	411	20.1 (25.3)	51.6	4.3 (5.4)	260.2	5.3
4_340_2	418	19.4 (20.2)	60.3	4.9 (5.1)	292.2	1.2
5_340_2	434	20.4 (20.4)	61.4	5.5 (5.5)	250.8	0.8

Note: '2' refers to CdS2 recipe.

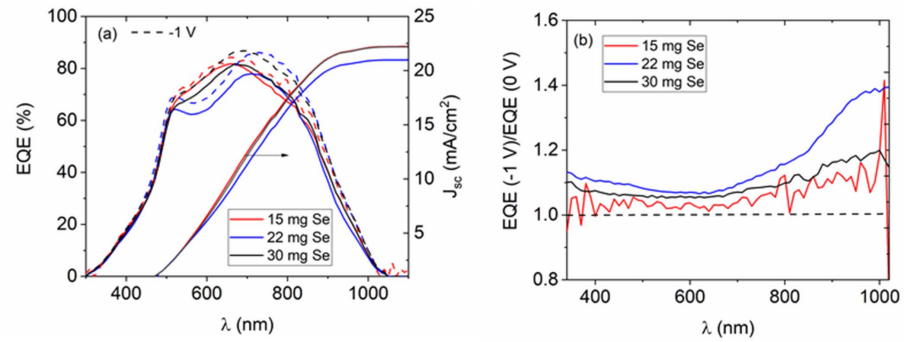

Figure 5. (a) EQE measurements of the PV devices of Series 1 measured under zero bias and under −1 V reverse bias. (b) EQE (−1 V)/EQE (0 V) ratio for the devices shown in (a).

The effect of selenization temperature on PV parameters is significant, as shown in table 3. Selenization temperature of 340 °C leads to the best-performing solar cells. As shown previously, a larger absorber grain size was obtained at this temperature. However, the device based on the Sb_2Se_3 layer selenized at 360 °C exhibits a much lower FF and J_{SC} due to its higher series resistance R_s and very low shunt resistance R_{sh}. The sample selenized at 360 °C corresponds to the absorber with the highest Se content, and the significant Se excess may have promoted the formation of Se_{Sb} antisite defects, which are detrimental to device performance [26]. In general, the devices performance of Series 2 is lower than that of Series 1. It is important to note the significant presence of Sb oxide in Series 2, which is detrimental to solar-cell efficiency, acting as recombination center and primarily reducing J_{SC}, as previously reported [22, 23].

3.3. Influence of CdS buffer layer on Sb_2Se_3 thin-film solar cells

Another aspect to take into account is the CdS buffer layer to develop the proper heterojunction. In the present work, two different CBD recipes were for the deposition of the CdS layer (see table 2).

XPS was used to characterize the chemical composition of the near-surface region of the CdS1 and CdS2 buffer layers. Figure 6 shows (a) the Cd 3d core level doublet, (b) the Cd MNN Auger transition and (c) the S 2p core level doublet spectra, respectively, after background subtraction based on the Tougaard method [16]. It should be noted that, after normalizing the spectra to the same maximum intensity, the Cd 3d core level, the Cd MNN Auger transition and the S 2p core level spectra of the two samples are nearly identical and no obvious differences can be observed between the two samples, CdS1 and CdS2. The Cd 3d core level can be fitted with two peaks accounting for the $d_{5/2}$ and $d_{3/2}$ contribution to the doublet with a spin–orbit splitting of 6.8 eV and imposing a theoretical $d_{5/2}/d_{3/2}$ area ratio of 1.5. Values of 405.42 and 405.49 eV are obtained for the binding energy of the $3d_{5/2}$ core level for CdS1 and CdS2 samples, respectively. For the Cd MNN Auger transition, values of 380.87 and 380.86 eV, are observed for the kinetic energy of the $M_4N_{45}N_{45}$ Auger peak for CdS1 and CdS2 samples, respectively. In contrast with the Cd 3d core level spectra, two different chemical species are observed in the S 2p

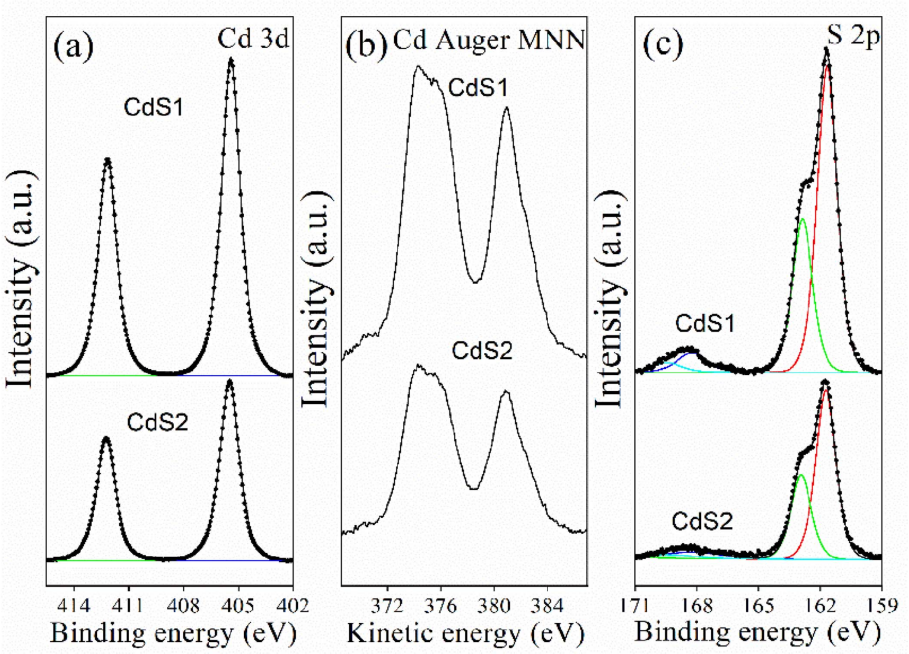

Figure 6. (a) Cd 3d core level doublet, (b) Cd MNN Auger transition and (c) S 2p core level doublet spectra, respectively, for the CdS1 and CdS2 thin films.

core level spectra. To reproduce the S 2p doublet of each chemical species, two peaks accounting for the $p_{3/2}$ and $p_{1/2}$ contribution to the doublet with a spin orbit splitting of 1.2 eV and imposing a theoretical $p_{3/2}/p_{1/2}$ area ratio of 2.0, have been used for each chemical species. For the more intense main feature, a value of 161.7 eV is obtained for the $2p_{3/2}$ binding energy in the two samples. This value is in good agreement with those reported in the literature for S^{2-} species belonging to CdS [28]. For the less intense secondary feature, observed at higher binding energies, a value of $\sim$ 168.2 eV is found for the $2p_{3/2}$ binding energy in both samples. This value is associated with sulfate species SO_4^{2-} [28].

The SO_4^{2-} species are detected in very small concentration in both CdS layers. Since CdS1 uses $CdSO_4$ as precursor whereas CdS2 uses $Cd(NO_3)_2$, the presence of sulfate species in both films indicates that they originate from surface oxidation during air exposure prior to XPS measurement rather than from precursor residues. The Cd modified Auger parameter, α', calculated as the sum of the Cd $3d_{5/2}$ binding energy and the kinetic energy of the Cd $M_4N_{45}N_{45}$ Auger transition, are 786.29 and 786.35 eV for CdS1 and CdS2 samples, respectively. The values observed for the Cd $3d_{5/2}$ binding energy, the Cd $M_4N_{45}N_{45}$ kinetic energy, the S $2p_{3/2}$ binding energy and α', are consistent with those reported in the literature for CdS [28]. Moreover, the measured α' values confirm the absence of other chemical species, such as metallic Cd, CdO or $Cd(OH)_2$ in the near-surface region of the films.

Figure 7(a) shows the total transmittance and total reflectance spectra of the CdS1 and CdS2 thin films deposited on SLG substrate. The CdS1 buffer layer exhibits a lower transmittance across the entire measured wavelength range, particularly between 300 and 500 nm. This decrease can be attributed to a reduction in the optical bandgap energy of the CdS1 layer. A direct optical bandgap energy was estimated from Tauc's plots with values of 2.31 and 2.40 eV for the CdS1 and CdS2, respectively. Figure S5 presents the total, straight-through, and diffuse transmittance, as well as total and diffuse reflectance of the CdS1 and CdS2 buffer layers. The higher total transmittance of CdS2 observed in figure 7(a) is primarily due to its higher straight-through transmittance, while the diffuse transmittance remains below 15% across the entire wavelength range. Although CdS1 exhibits higher total reflectance than CdS2, the diffuse reflectance is similar for both layers. For this investigation, and based on the previous results shown above, the Sb_2Se_3 absorber layer was prepared by selenization of Sb layer at 340 °C for 60 min and adding 25 mg Se (Series 3 in table 1). Once again, after the selenization process a Sb_2Se_3 film with preferential orientation in the [*kk*1] direction is obtained, free of pinholes and forming a compact Sb_2Se_3/Mo back structure. A minor contribution of Sb_2O_x co-exists with Sb_2Se_3 phase, as determined by FTIR measurements (see figure S4). In comparison with sample 2_340, the absorber 3_340 presents significantly less antimony oxide, which correlates with the higher integrated J_{SC} value of the device 3_340 (see table 3). The modification of the CdS buffer layer has a significant impact on all

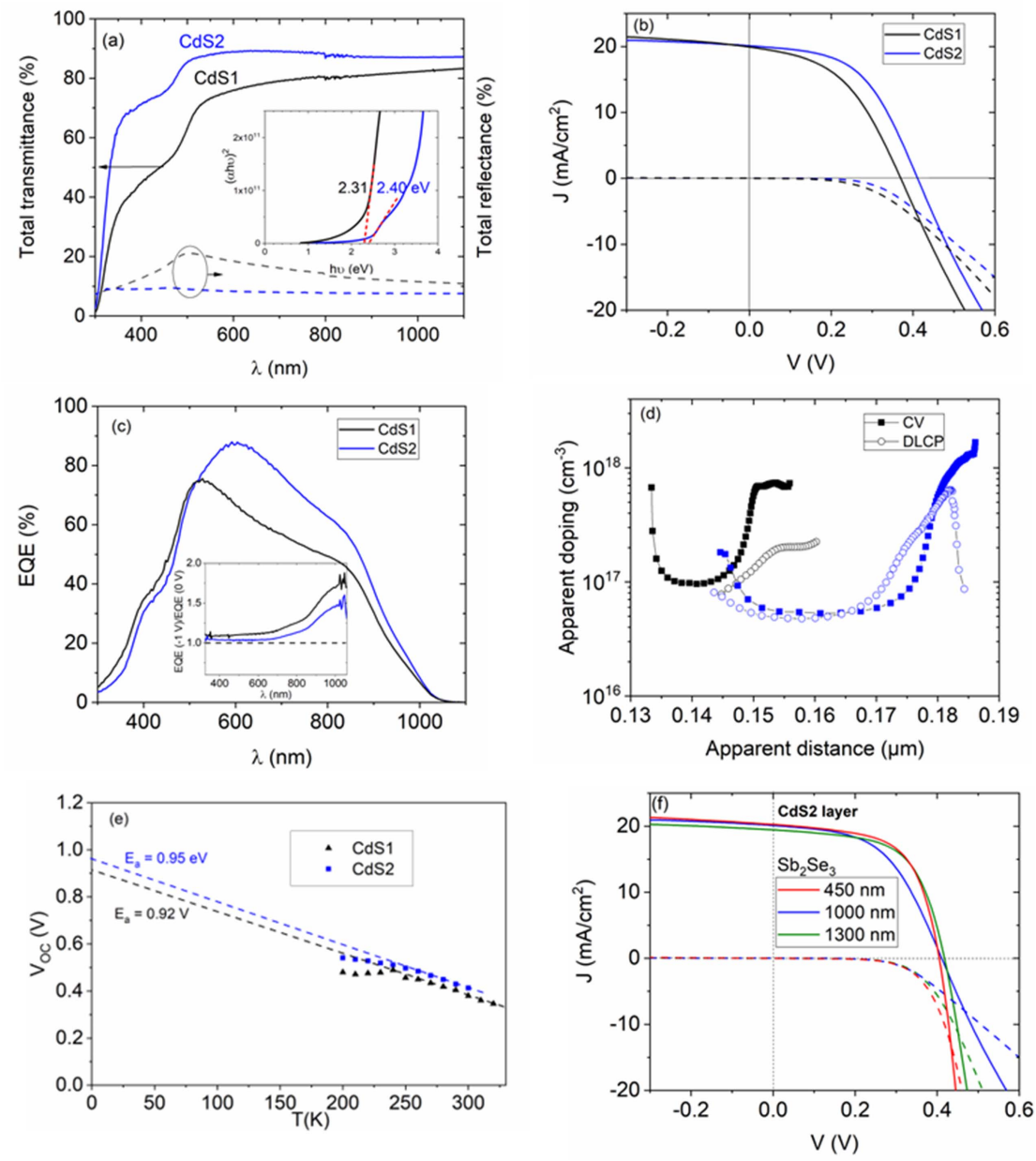

Figure 7. (a) The total transmittance (left axis) and total reflectance (right axis) spectra of CdS1 and CdS2 buffer layers. Inset is the Tauc´s plot deduced from the transmittance spectrum. (b) *J*–*V* characteristics under illumination (solid lines) and in the dark (dashed lines), (c) EQE measurements with EQE (−1 V)/EQE (0 V) ratio, (d) DLCP and CV measurements and (e) V_{OC}–*T* profiles for the solar cells of Series 3 using CdS1 (black) and CdS2 (blue) buffer layers. (f) *J*–*V* characteristic under illumination (solid lines) and in the dark (dashed lines) of Sb_2Se_3-based PV devices with different thickness of the absorber using the CdS2 buffer layer.

the PV parameters, achieving a V_{OC} of 411 mV and an efficiency of 5.3% (active area) versus 370 mV and 3.6% (active area) for CdS2 and CdS1 buffers, respectively (see table 3). *J*–*V* characteristics, EQE, *C*–*V* and DLCP measurements of the best-performing devices from Series 3 are plotted in figure 7. Although the CdS2 recipe led to improved device performance, a cross-over effect observed in the *J*–*V* curves indicates that the heterointerfaces are not yet fully optimized [13]. The EQE measurements under applied bias demonstrate that the photogenerated carriers are not completely collected, particularly when using the standard CdS1 buffer layer. As shown in figure 7(c), the strong absorption of the CdS in the short-wavelength region (300–500 nm) reduces the incident light utilization of Sb_2Se_3 absorber layer. Moreover, the higher total reflectance of the CdS1 film contributes to a lower EQE for wavelength higher than 500 nm (see figure 7(a) and S5). The CdS thickness measured by TEM is approximately 45 nm for the CdS1 layer and 60 nm for the CdS2 layer, which may also account for the reduced short-wavelength spectral response observed in the CdS2-based device. The modification of the Sb_2Se_3-based PV devices

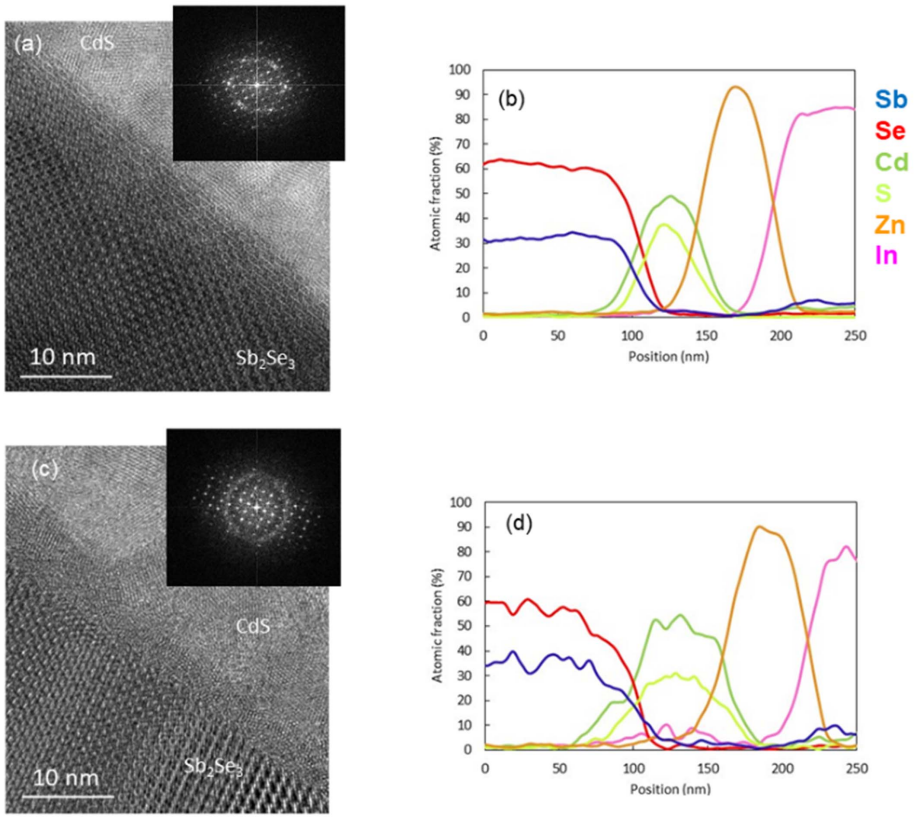

Figure 8. (a) and (c) HRTEM images of Sb_2Se_3/CdS/ZnO structure together with the FFT corresponding to the CdS layers, (b) and (d) EDX depth profiles of the Sb, Se, Cd, S, Zn, In elements for the PV-devices using CdS1 and CdS2 buffer layers respectively.

by the variation of the buffer layer results in lower defects concentration, N_{CV} of 7.9 × 10^{16} cm^{-3} and 2.0 × 10^{17} cm^{-3} for CdS2 and CdS1 solar cells, respectively. Moreover, the interfacial defect density N_i of 5.1 × 10^{16} cm^{-3} and 1.4 × 10^{17} cm^{-3} were obtained for CdS2 and CdS1-based PV devices, indicating a better heterojunction for the device with CdS2 buffer layer. A wider space charge region W_d = 175 nm is also obtained for the modified (CdS2) solar cell compared to W_d = 149 nm for the standard CdS1 device, which implies more efficient charge-carrier collection, consistent with the higher J_{SC} value.

Furthermore, temperature-dependent V_{OC} (V_{OC}–T) was analyzed to explore the activation energy (E_a) of the dominant recombination mechanism, as described by the following equation:

$$V_{OC} = \frac{E_a}{q} - \frac{Ak_BT}{q}\ln\left(\frac{J_0}{J_L}\right) \quad (2)$$

where q is the elementary charge, T is the absolute temperature, k_B is Boltzmann's constant, J_0 is reverse saturation current, and J_L is the photocurrent. In general, two major recombination mechanisms commonly exist in PV devices: (i) space-charge-region recombination-dominated, for which $E_a = E_g$ and (ii) interface-recombination-dominated, for which $E_a < E_g$ [29]. In figure 7(e) E_a is by extrapolation of V_{oc} to 0 K using equation (2). Both solar cells exhibit significantly lower E_a values compared to their respective bandgap values of 1.24 eV derived from EQE displayed in figure 7(c). This indicates that interface recombination is the dominant recombination mechanism in these devices, regardless of the CdS buffer layer used.

Figure 8 shows the cross-sectional HRTEM image of the CdS/Sb_2Se_3 heterointerface. The fast Fourier transform (FFT) corresponding to each CdS image has also been included. As mentioned above, the CdS2 layer is not only thicker, but also exhibits a more amorphous and less compact structure. This can be clearly inferred from the TEM image and from the FFT, where a circle typically related to amorphous layer is clearly observed. As shown in figure 7(a) and figure S5, CdS2 presents a higher transmittance and a higher bandgap energy than CdS1, in agreement with a more amorphous structure. In addition, the EDX depth profiles of the completed devices (see figures 8(b) and (d)) show a significant Cd diffusion towards the absorber layer in the case of the CdS2 buffer layer. It is known that the Sb_2Se_3/CdS

heterojunction plays a crucial role in the thin-film solar cells performance. The enhanced Cd diffusion into the Sb_2Se_3 layer using the CdS2 buffer layer results in a lower defect density at the interface as determined from *C–V* and DLCP measurements. Cao *et al* [7] reported that Ag doping of CdS promotes the Cd diffusion into the absorber layer, forming Cd_{Sb} antisite defects, that reduce the density of deep-level centers. It has also been demonstrated that the diffusion of Cd into Sb_2Se_3 introduces interstitial Cd_i defects, which act as donors and form a buried homojunction within the CdS/Sb_2Se_3, therefore dictating charge separation and overall device performance [30]. Similar effects may also occur in the present devices without the need for introducing any external dopants. In our case, the more amorphous nature of CdS2, likely facilitates Cd mobility during the process, enabling a higher concentration of Cd to diffuse into the absorber. On the other hand, examination of the Sb_2Se_3/Mo back interface reveals that Se diffuses towards the Mo layer. The selenization temperature of 340 °C and the preferred film orientation are enough to provide favorable diffusion pathways for Se atoms. A Se-rich region at the bottom of the Sb_2Se_3 film promotes the formation of an ∼80 nm-thick $MoSe_2$ layer at the back contact, as shown in figure S6 of the supplementary information. The formation of this $MoSe_2$ layer during the selenization of Sb layer is commonly observed in such processes and generally ensures an efficient ohmic back contact [13, 21].

3.4. Electronic properties of Sb_2Se_3, CdS films and solar cell devices

To study the electronic properties of the Sb_2Se_3 and CdS films, as well as of the Sb_2Se_3/CdS heterointerface, the KP and PYS measurements were performed. Absolute values of the work function (WF or Φ) and ionization energies (IE or E_i), which define the positions of the Fermi level (E_F) and the valence band maximum (E_{VBM}) relative to the local vacuum level, were determined from the KP and PYS measurements, respectively. The conduction band minimum (E_{CBM}) was calculated as $E_{CBM} = E_{VBM} + E_g$ by using the bandgap values of the respective films determined in the previous sections. The E_{CBM} value relative to the vacuum level defines the electron affinity (E_A).

For the Sb_2Se_3 films, the KP and PYS measurements reveal nearly identical electronic properties irrespective of the used SLG or Mo/SLG substates (see figure 9). The work functions measured in figure 9(a) under dark conditions are in the range of 5.00–5.02 eV. Assuming flat-band conditions achieved under illumination, the bulk work function (Φ) values are $\Phi = 5.12$ eV and $\Phi = 5.15$ eV for the films deposited on SLG and Mo/SLG substrates, respectively. According to the SPV analysis described in the experimental section, the positive SPV values recorded in figure 9(b) between 0.118–0.123 V indicate *p*-type conductivity of the as-deposited Sb_2Se_3 layers. Considering the IEs determined from figure 9(c) and thus the E_{VBM} of 5.28–5.31 eV, and the bulk WFs which were determined above, we find a VBM offset with respect to the Fermi level (E_F–E_{VBM}) of 0.16–0.17 eV. Using this E_F–E_{VBM} value, we calculated the equilibrium hole concentration (*p)* in the as-prepared Sb_2Se_3 thin films using the following equation:

$$p = N_V \exp\left[-\left(E_F - E_{VBM}\right)/kT\right] \tag{3}$$

where $N_V \equiv 2\left(2\pi m_h kT/h^2\right)^{3/2}$ is the effective density of states in the valence band, k is Boltzmann´s constant, T is the absolute temperature, m_h is the density-of-state effective mass of holes in the valence band and h is the Planck constant [31]. We consider $m_{h\_Sb2Se3} = 0.198m_0$, where m_0 is the free electron rest mass [32], and obtain $p_{Sb2Se3} = 3.7 \times 10^{15}$ cm^{-3}. Using the band-gap energy $E_{g\text{-}Sb2Se3} = 1.24$ eV determined from the EQE measurements, we obtain the CBM position, and hence the $E_A = 4.07$ eV. Note that the obtained values for the CBM and VBM positions are in a reasonable agreement with the previously reported calculated data [32]. The work functions as well as the E_{CBM} and E_{VBM} values with respect to vacuum level are summarized in the energy level diagrams in figure 9(d).

The electronic parameters of the CdS1 and CdS2 thin films were investigated in their as-deposited state on top of the Sb_2Se_3/Mo/SLG stacks. The work functions measured under dark conditions show a difference of approximately 0.25 eV (see figure 10(a)). To determine the bulk WFs, the samples were illuminated with blue light having a photon energy of 3.06 eV, which is higher than the respective bandgap energies $E_{g\_CdS1} = 2.31$ eV and $E_{g\_CdS2} = 2.40$ eV, thereby generating charge carriers only in the top region of the CdS layers. The SPV plots (see figure 10(b)) display negative SPV signals, which confirm that the photoresponse originates from the *n*-type CdS layers. It should be noted that the charge-carrier generation and separation dynamics under illumination differ significantly between the two samples. A sharp SPV rise is observed for the CdS2 layer, while a more gradual (monotonic) increase is recorded for the CdS1 films. This denotes a better passivated CdS2 film surface with less defects compared to CdS1 layer. Ionization energies of 6.00 eV and 6.08 eV were determined for CdS1 and CdS2, respectively, from photoelectron yield spectra shown in figure 10(c), which match well the

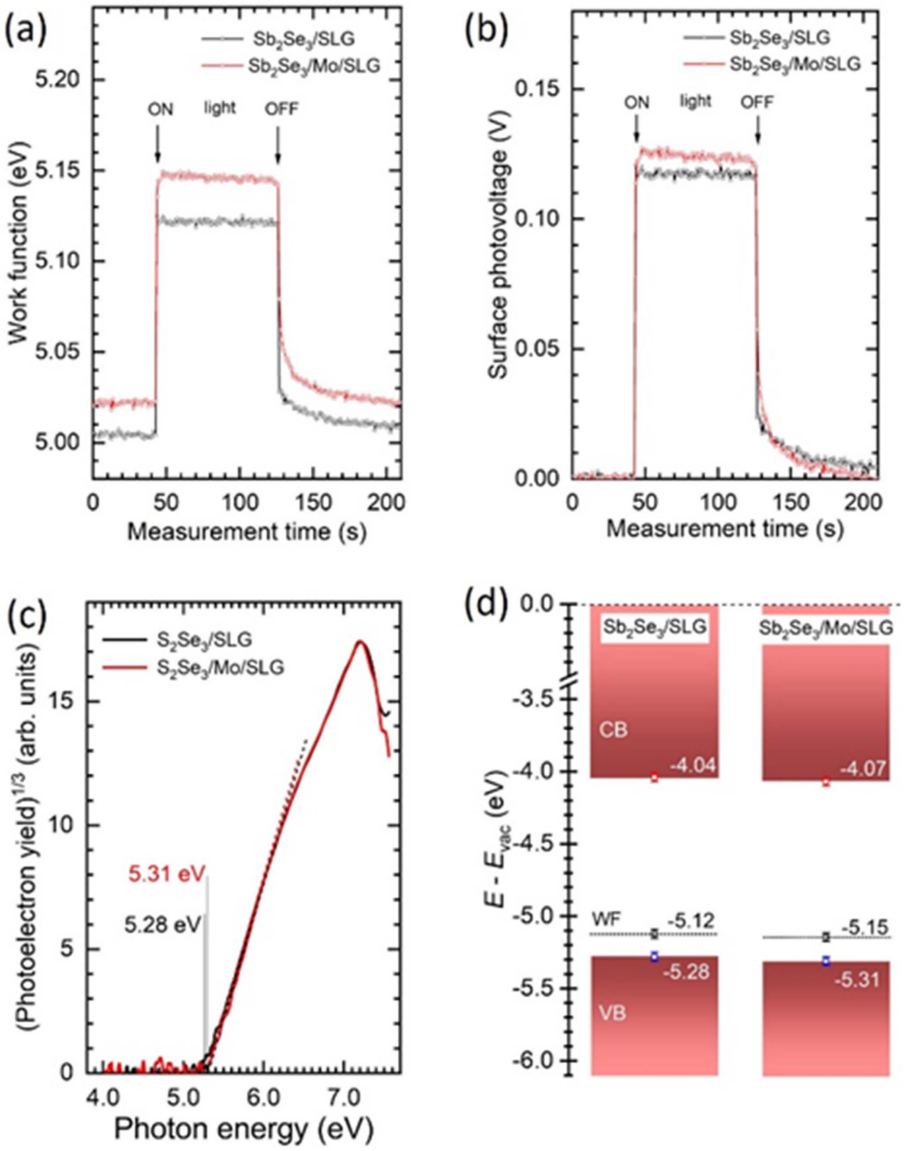

Figure 9. (a) Work function of Sb_2Se_3 thin films measured in the dark and under illumination with a continuous-wave (cw) laser at 670 nm and an incident power density of 100 mW cm^{-2}. (b) Surface photovoltage signals. (c) Photoelectron yield spectra with the corresponding ionization energies. (d) Energy-level diagrams of Sb_2Se_3 thin films deposited on SLG and Mo/SLG substrates.

previously reported values for CdS [17, 33]. With the defined VBM positions and the CdS bandgaps determined above, similar CBM positions and electron affinities of 3.68 eV were calculated. Further, E_{CBM}–E_F values were calculated for both CdS layers. With E_{CBM}–E_F = 0.35 eV under flat-band conditions for CdS2 and $m_{e\_CdS} = 0.25m_0$ [33], and by applying Boltzmann statistics for *n*-type CdS, we obtain an electron concentration of $n_{CdS2} = 1.61 \times 10^{11}$ cm^{-3}. The latter charge carrier concentration denotes an intrinsic property of the CdS2 film pointing at a stoichiometric CdS with thus less defects [34]. For CdS1, with E_{CBM}–E_F = 0.25 eV, we obtain $n_{CdS1} = 2.31 \times 10^{14}$ cm^{-3}. The lower charge carrier concentration in CdS2 layer will, consequently, largely extend the space-charge region in the CdS buffer, resulting in enhanced charge separation and reduced recombination probability. In addition, the expected higher resistivity of the CdS2 films is likely to mitigate possible pinholes between the front and back contacts of the solar cells. As a result, higher parallel resistances and FFs are anticipated—consistent with the experimental data presented in table 3. All calculated energy levels for the CdS1 and CdS2 films are summarized in the band alignment diagram displayed in figure 10(d).

With the known energy levels of the Sb_2Se_3 absorber and CdS buffer layers, we calculated the corresponding band bending potentials and band offsets at the CdS/Sb_2Se_3 heterointerface, yielding a total band bending potential in the depletion region

$$V_D = V_{D\_Sb2Se3} + V_{D\_CdS} = WF_{Sb2Se3} - WF_{CdS} \quad (4)$$

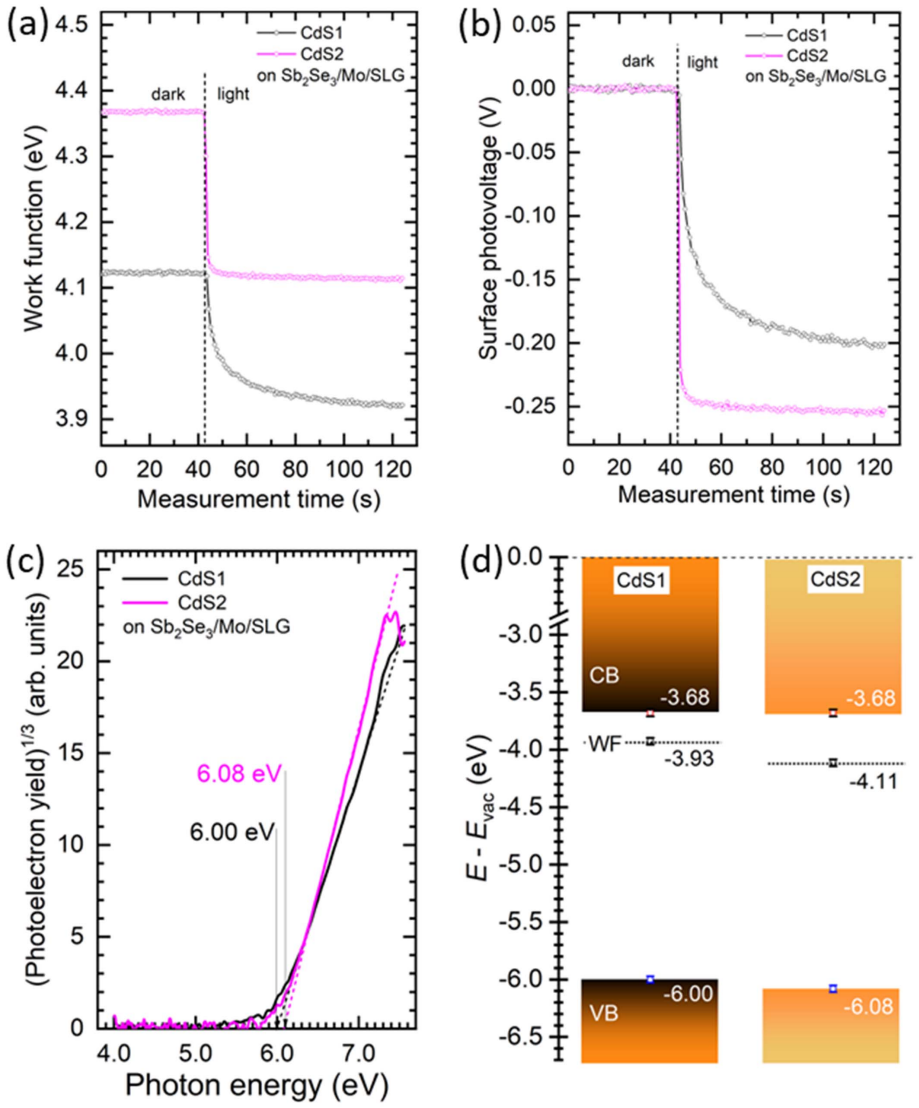

Figure 10. (a) Work function of CdS1 and CdS2 thin films measured in the dark and under illumination with a continuous-wave (cw) laser of 405 nm at an incident power density of 100 mW cm^{-2}, (b) surface photovoltage responses, (c) photoelectron yield spectra with the ionization energies determined from the photoemission onset, and (d) energy level diagrams of CdS1 and CdS2 thin films deposited on Sb_2Se_3/Mo/SLG substrates.

the CBM band offset

$$\Delta E_{\mathrm{CBM}} = E_{\mathrm{A_{Sb2Se3}}} - E_{\mathrm{A_{CdS}}} \tag{5}$$

and the VBM band offset

$$\Delta E_{\mathrm{VBM}} = IE_{\mathrm{CdS}} - IE_{\mathrm{Sb2Se3}}. \tag{6}$$

We calculated a V_{D} of $\approx$ 1.20 V and $\approx$ 1.03 V at the CdS1/Sb_2Se_3 and CdS2/Sb_2Se_3 interfaces, respectively. For the calculation of the $V_{\mathrm{D\_Sb2Se3}}$, we used the following equation:

$$V_{\mathrm{D}_p} = V_{\mathrm{D}} N_{\mathrm{D}} / (N_{\mathrm{A}} + N_{\mathrm{D}}) \tag{7}$$

where N_{D} and N_{A} are the n-type and p-type dopant densities, respectively [35]. Using the electron and hole concentrations determined above for the CdS and Sb_2Se_3 layers, we obtain $V_{\mathrm{D\_Sb2Se3}} = 0.07$ V or the device incorporating the CdS1 buffer layer. For comparison, we also calculated $V_{\mathrm{D\_Sb2Se3}}$ by applying the following expression:

$$V_{\mathrm{D}_p} = eN_{\mathrm{A}} W_{\mathrm{D}_p}^2 / 2\varepsilon_{\mathrm{o}}\, \varepsilon_{r-p} \tag{8}$$

where e is the elementary charge, W_{Dp} is the depletion region width in the p-type layer, ε_o is the vacuum permittivity and ε_{r-p} is the relative dielectric constant of the p-type semiconductor. Using $W_D = 149$ nm, as obtained from the C–V measurements in section 2.3 for the devices with CdS1, and $\varepsilon_{r\text{-}Sb2Se3} = 15$ [36, 37], we obtained $V_{D\_Sb2Se3} = 0.05$ V, which is in good agreement with the value calculated above. By using $W_{D\_Sb2Se3} = 175$ nm, determined for the CdS2-based devices from electrical measurements, we calculated $V_{D\_Sb2Se3} = 0.07$ V. Thus, the solar cells with the CdS2 buffer exhibit, in addition to a wider space-charge region within Sb_2Se_3, a stronger downwards band bending. While the former enhances the carrier collection length, the latter contributes to an increased device V_{oc}. The band bending potentials in the CdS1 and CdS2 were calculated to be 1.15 V and 1.03 V, respectively. We note that for achieving a similar V_{D_Sb2Se3} of 0.07 V by using equation (7), the concentration of acceptors in Sb_2Se_3 must be adjusted to 2.2×10^{12} cm^{-3}, which is by several orders of magnitude lower than the value obtained for the Sb_2Se_3 bulk. This suggests that the CdS2/Sb_2Se_3 interface undergoes electronic changes during the CBD deposition of CdS2, consistent with the observed diffusion of Cd into the Sb_2Se_3 absorber as revealed by EDX depth profiling, and having the effect of introducing an interstitial Cd_i donor level. The Cd_i donors compensate the acceptors in Sb_2Se_3 leading to a decreased carrier concentration and even result in its conversion into n-type conductivity [30]. Furthermore, it should be emphasized that the inversion of the conductivity type of the Sb_2Se_3 surface at the CdS2/Sb_2Se_3 interface will lead to a decrease of the recombination rate and, consequently, in a higher open circuit voltage, which is in fact observed. A detailed investigation of the CdS2/Sb_2Se_3 interface is in focus of our future studies.

Similar CBM band offsets (ΔE_{CBM}) of 0.36 eV corresponding to a spike-type alignment were calculated for both CdS1/Sb_2Se_3 and CdS2/Sb_2Se_3 interfaces. For ΔE_{VBM} we found values of 0.72 eV and 0.77 eV for the CdS1/Sb_2Se_3 and CdS2/Sb_2Se_3 interfaces, correspondingly. As consequence, the CBM and VBM band offsets are expected to have similar effects on the electronic transport through both buffer/-absorber interfaces.

SPV measurements were performed on complete ITO/ZnO/CdS/Sb_2Se_3/Mo/SLG solar cells at room temperature under white light illumination (5700 K color spectrum and 100 mW cm^{-2}). The devices with CdS1 showed an SPV of 0.373 ± 0.002 V, whereas the solar cells with CdS2 recorded an SPV of 0.413 ± 0.002 V (see figure S7 in the supplementary information). These results are in excellent agreement with the devices V_{oc}-s measured under the simulated sun light.

Once the electronic properties of the heterointerface had been investigated, the CdS2 buffer layer was employed to fabricate solar cells with thinner and thicker Sb_2Se_3 absorbers, of around 450 and 1300 nm under the same selenization conditions as those used for Series 3. As shown in table 3, these devices are characterized by the highest FF, achieving a total efficiency of 5.5% for the thinnest (450 nm) absorber layer. These results highlight two issues independent from the absorber thickness. First, the selenization temperature of 340 °C leads to improved efficiency of the solar cells, and second, the CdS buffer layer plays a key role in enhancing the heterojunction quality, with reduced defect density and enhanced PV parameters. However, the cross-over effect observed in the J–V characteristics in figure 7(f) indicates that there is still a lot of room to improve the different interfaces. It has been observed that the formation of $MoSe_2$ at the back interface is induced by the selenization process, and, that enhanced solar cells have been achieved via the use of CdS2, however, the interface recombination indicates that further investigation to optimize the heterointerface is necessary. From these experimental findings, it is important to emphasize that the absorber thickness is not the dominant factor governing device performance, as it can be reduced to 450 nm without any efficiency loss.

4. Conclusions

Sb_2Se_3 absorber thin films and CdS buffer layers were synthesized, and complete devices with ITO/ZnO/CdS/Sb_2Se_3/Mo/SLG substrate configuration were fabricated. The Sb_2Se_3 films were prepared by selenization of Sb precursor on Mo/SLG substrates in a quasi-closed graphite box. Optimum electronic quality of the Sb_2Se_3 films was achieved when an appropriate Se amount, matched the graphite box volume, was used at selenization temperature of 340 °C. The resulting Sb_2Se_3 films are orientated in the [hk1] direction, predominantly in the (002) plane. As determined by SPV, combined KP and PYS measurements, the Sb_2Se_3 thin films exhibit p-type conductivity with a doping concentration of approximately 4×10^{15} cm^{-3}. The VBM is located 5.28 eV below the vacuum level, and considering a bandgap energy of 1.24 eV, the E_A is calculated to be 4.04 eV.

CdS layers were deposited by the CBD method using two recipes: (i) a standard recipe commonly used for conventional solar cells and (ii) a developed recipe based on solutions of $Cd(NO_3)_2$, sodium citrate and thiourea at low concentrations. CdS1 films deposited by the standard recipe exhibit a

bandgap of 2.31 eV, while the CdS2 layers prepared by the new CBD recipe show an increased bandgap of 2.40 eV, as determined from UV–vis measurements. Although the CdS2 films show a similarly low diffuse reflectance compared to the CdS1 layers, they exhibit higher transmittance across the entire 300–1100 nm wavelength range and a total reflectance reduced by approximatively 15% in 450–800 nm region. Electron concentrations obtained from KP-PYS measurements are 2.31×10^{14} cm^{-3} and 1.61×10^{11} cm^{-3} for the CdS1 and CdS2 films respectively, with the later value being characteristic of stoichiometric 1:1 CdS. These results demonstrate the superior optoelectronic properties of the CdS2 films relative to the CdS1 layers.

The incorporation of CdS2 in ITO/ZnO/CdS/Sb_2Se_3/Mo/SLG solar cells results in power conversion efficiencies of 5.4% versus 3.6% of the devices with CdS1. This improvement is attributed to the superior optoelectronic properties of the CdS2. In addition, the observed Cd diffusion toward the absorber layer suggests the formation of interstitial Cd_i donors, which contribute to a stronger downward band bending at the buffer/absorber interface, therefore reducing interface recombination and increasing the open circuit voltage. Band-bending calculations indicates that achieving the potential in Sb_2Se_3 within CdS2-based devices requires acceptors concentration lower than that measured in Sb_2Se_3 bulk, consistent with the presence of Cd_i donors at the CdS2/Sb_2Se_3 interface. The SPV measurements of the complete devices are in excellent agreement with the devices V_{OC}-s obtained under simulated sunlight, further confirming the higher open circuit voltage of the CdS2-buffered solar cells.

EQE measurements indicate a limited charge carrier collection length in the devices. To mitigate this, the absorber thickness was reduced to 450 nm, leading to a total area efficiency of 5.5%.

In conclusion, although the new CBD-CdS2 recipe enables the fabrication of devices with improved efficiencies, further optimization of the band alignment at the buffer/absorber interface remains essential. This requires a detailed investigation of the chemical and electronic structure of the CdS/Sb_2Se_3 interface and the development of targeted strategies for its improvement, which constitute the focus of our ongoing studies. Overall, these results highlight the critical importance of optimizing the CdS/Sb_2Se_3 heterojunction to achieve further enhancement in device performance.

Data availability statement

All data that support the findings of this study are included within the article (and any supplementary files).

Supplementary data 1 available at http://doi.org/10.1088/2515-7655/ae3d63/data1.

Acknowledgments

This work was funded by CETPartnership, the Clean Energy Transition Partnership under the 2023 joint call for research proposals (SUNLIFE, CETP-FP-2023-00137), co-funded by the European Commision (GA N° 10169750) and with the following funding organization (PCI2024-155033-2 funded by MICIU/AEI/10.13039/501100011033/UE and TK210 GREENTECH funded by Estonian Research Council). This work was also supported by ASSESS (TED2021-129666B-C21 and TED2021-129666B-C22) project funded by MCIN/AEI/10.13039/501100011033 and by the 'European Union Next Generation EU/PRTR', InnoPV (PID 2022-140226OB-C3) funded by MICIU/AEI/10.13039/501100011033 and by 'FEDER/UE' and MAS-PV (ILINK23057) funded by CSIC and RENEW-PV project from COST (European Cooperation in Science and Technology) Action Research and International Networking on Emerging Inorganic Chalcogenides for Photovoltaics (CA21148). Authors would also like to acknowledge projects 2DEnLight (PID2020-113415RB-C21) and LAB (PID2023-150420NB-C33) projects funded by Spanish MICINN, NO-DEPENDENCE (G6037) financed by NATO SPS Programme. The authors would like to acknowledge the Research Foundation Flanders-Hercules Foundation (Belgium) (FWO-Vlaanderen, project No AUGE/13/16:FT-IMAGER). B Galiana is member of the Institute of Chemistry and Materials Technology 'Álvaro Alonso Barba' of the UC3M. STEM measurements were partially carried out though an ELECMI-2023 call. We also acknowledge the service from the MiNa Laboratory at IMN-CSIC, and funding from CM (project S2018/NMT-4291 TEC2SPACE), MINECO (project CSIC13-4E-1794) and EU (FEDER, FSE). The Raman experiments were performed in the Laboratory for Solid State Physics, headed by Dr Nenad Lazarević, at the Institute for Physics Belgrade, University of Belgrade, Serbia.

Author contributions

David Payno 0000-0003-1381-5121
Formal analysis (supporting), Investigation (supporting), Methodology (supporting)

Yudania Sánchez
Investigation (supporting), Methodology (equal), Resources (lead)

Marin Rusu 0000-0002-1429-0219
Data curation (equal), Formal analysis (equal), Investigation (equal), Methodology (equal), Resources (lead), Writing – original draft (supporting), Writing – review & editing (equal)

Luna Lázaro-Castrillón 0009-0003-8820-8999
Data curation (supporting), Investigation (supporting)

Samira Khelifi
Formal analysis (equal), Investigation (supporting), Methodology (equal), Resources (lead), Writing – review & editing (equal)

Beatriz Galiana
Data curation (equal), Formal analysis (equal), Methodology (supporting), Resources (lead), Writing – review & editing (supporting)

Víctor Bonal
Data curation (supporting), Investigation (equal)

Sanja Djurdjić Mijin 0000-0002-4597-8219
Formal analysis (equal), Methodology (supporting), Resources (lead), Writing – review & editing (supporting)

Antonio Arranz 0000-0001-6434-189X
Data curation (equal), Formal analysis (equal), Methodology (supporting), Resources (lead), Writing – original draft (supporting)

Mati Danilson
Data curation (equal), Methodology (supporting), Resources (lead)

Snežana Lazić 0000-0002-1389-1901
Data curation (supporting), Funding acquisition (lead), Methodology (supporting), Resources (equal), Writing – review & editing (supporting)

Maarja Grossberg-Kuusk 0000-0003-3357-189X
Funding acquisition (lead), Methodology (supporting), Resources (equal), Writing – review & editing (supporting)

Thomas Unold
Resources (lead), Validation (supporting)

Rosalia Serna
Funding acquisition (lead), Resources (lead), Writing – review & editing (supporting)

José Manuel Merino
Funding acquisition (lead), Resources (supporting), Writing – review & editing (supporting)

Raquel Caballero 0000-0003-0215-7311
Conceptualization (lead), Formal analysis (lead), Funding acquisition (lead), Investigation (lead), Methodology (lead), Project administration (lead), Resources (lead), Supervision (lead), Validation (lead), Writing – original draft (lead), Writing – review & editing (lead)

References

[1] Shah U A, Chen S, Khalaf G M G, Jin Z and Song H 2021 Wide bandgap Sb_2S_3 solar cells *Adv. Funct. Mater.* **31** 2100265
[2] Zhao Y *et al* 2022 Regulating deposition kinetics via a novel additive-assisted chemical bath deposition technology enables fabrication of 10.57%- efficiency Sb_2Se_3 solar cells *Energy Environ. Sci.* **15** 5118
[3] Duan Z *et al* 2022 Sb_2Se_3 thin-film solar cells exceeding 10% power conversion efficiency enabled by injection vapor deposition technology *Adv. Mater.* **34** 2202969

[4] Jiménez-Guerra M *et al* 2025 Synergistic effects of high-pressure processing and interface engineering in Sb_2Se_3/CdS photovoltaic devices *Sol. Energy* **298** 113670
[5] Liang G, Chen M, Ishaq M, Li X, Tang R, Zheng Z, Su Z, Fan P, Zhang X and Chen S 2022 Crystal growth promotion and defects healing enable minimum open-circuit voltage deficit in antimony selenide *Sol. Cells Adv. Sci.* **9** 2105142
[6] Zhou Y *et al* 2015 Thin-film Sb_2Se_3 photovoltaics with oriented one-dimensional ribbons and benign grain boundaries *Nat. Photon.* **9** 409
[7] Cao Z, Shao B, Ye Z, Liu C, Li Z, Dong J, Wang W, Li J, Liu H and Zhang Y 2025 Anomalous electron doping in CdS to promote the efficiency improvement in Sb_2Se_3 thin film solar cells *Adv. Funct. Mater.* **35** 2418974
[8] Don C H *et al* 2023 Multi-phase sputtered TiO_2-Induced current–voltage distortion in Sb_2Se_3 solar cells *Adv. Mater. Interfaces* **10** 2300238
[9] Luo Y-D *et al* 2022 Energy band alignment for Cd-free antimony triselenide substrate structured solar cells by Co-sputtering ZnSnO buffer layer *Sol. Energy Mater. Sol. Cells* **240** 111721
[10] Zhang Z, Hu M, Jia T, Du J, Chen C, Wang C, Liu Z, Shi T, Tang J and Leng Y 2021 Suppressing the trapping process by interfacial charge extraction in antimony selenide heterojunctions *ACS Energy Lett.* **6** 1740
[11] Chen G, Luo Y, Abbas M, Ishaq M, Zheng Z, Chen S, Su Z, Zhang X, Fan P and Liang G 2024 Suppressing buried interface nonradiative recombination losses toward high-efficiency antimony triselenide solar cells *Adv. Mater.* **36** 2308522
[12] Jin M, Feng Z, Zhang J, Guo H, Jia X, Su J, Qiu J, Yuan N and Ding J 2021 Enhancement in the efficiency of Sb_2Se_3 solar cell with the adding of high electrical concentration CdS:Al film *Physica B* **619** 413211
[13] Lázaro-Castrillón L, Sánchez Y, Payno D, Razi U, Bonal V, Cabello F, Galiana B, Pérez-Rodríguez A, Merino J M and Caballero R 2025 Investigation of Cd-free Sb_2Se_3 thin-film solar cells by ALD-ZnSnO electron transport layer *Proc. 42nd European Photovoltaic Solar Energy Conf. and Exhibition* p 020085
[14] Neuschitzer M, Sánchez Y, López-Marino S, Xie H, Fairbrother A, Placidi M, Haass S, Izquierdo-Roca V, Pérez-Rodríguez A and Saucedo E 2015 Optimization of CdS buffer layer for high-performance $Cu_2ZnSnSe_4$ solar cells and the effects of light soaking: elimination of crossover and red kink *Prog. Photovolt., Res. Appl.* **23** 1660
[15] Ruiz-Perona A, Gurieva G, Sun M, Kodalle T, Sánchez Y, Grossberg M, Merino J M, Schorr S, León M and Caballero R 2021 Routes to develop a [S]/([S]+[Se]) gradient in wide band-gap $Cu_2ZnGe(S, Se)_4$ thin-film solar cells *J. Alloys Compd.* **868** 159253
[16] Fairley N *et al* 2021 Systematic and collaborative approach to problem solving using x-ray photoelectron spectroscopy *Appl. Surf. Sci. Adv.* **5** 100112
[17] Rusu M, Kodalle T, Choubrac L, Barreau N, Kaufmann C A, Schlatmann R and Unold T 2021 Electronic structure of the CdS/Cu(In,Ga)Se_2-interface of KF and RbF-treated samples by kelvin probe and photoelectron yield spectroscopy *ACS Appl. Mater. Interfaces* **13** 7745
[18] Dedova T *et al* 2025 Sb_2S_3 solar cells with TiO_2 electron transporting layers synthesized by ALD and USP methods *Sol. Energy Mater. Sol. Cells* **280** 113279
[19] Huang M, Xu P, Han D, Tang J and Chen S 2019 Complicated and unconventional defect properties of the quasi-one-dimensional photovoltaic semiconductor Sb_2Se_3 *ACS Appl. Mater. Interfaces* **11** 15564
[20] Kim J, Ji S, Jang Y, Jeong G, Choi J, Kim D, Nam S-W and Shin B 2021 Importance of fine control of se flux for improving performances of Sb_2Se_3 Solar cells prepared by vapor transport deposition *Sol. RRL* **5** 2100327
[21] Wen X, Lu Z, Yang X, Chen C, Washington M A, Wang G-C, Tang J, Zhao Q and Lu T-M 2023 Vertically aligned one-dimensional crystal-structured Sb_2Se_3 for high-efficiency flexible solar cells via regulating selenization kinetics *ACS Appl. Mater. Interfaces* **15** 22251
[22] Wang Z, Bae S, Baljozovic M, Adams P, Yong D, Service E, Moehl T, Niu W and Tilley S D 2024 One-step hydrothermal synthesis of Sn-Doped Sb_2Se_3 for solar hydrogen production *ACS Catal.* **14** 9877
[23] Liu D, Tang R, Ma Y, Jiang C, Lian W, Li G, Han W, Zhu C and Chen T 2021 Direct hydrothermal deposition of antimony triselenide films for efficient planar heterojunction solar cells *ACS Appl. Mater. Interfaces* **13** 18856
[24] Luo Y-D *et al* 2020 An effective combination reaction involved with sputtered and selenized Sb precursors for efficient Sb_2Se_3 thin film solar cells *Chem. Eng. J.* **293** 124599
[25] Liu X *et al* 2017 Enhanced Sb_2Se_3 solar cell performance through theory-guided defect control *Prog. Photovolt., Res. Appl.* **25** 861
[26] Savory C N and Scanlon D O 2019 The complex defect chemistry of antimony selenide *J. Mater. Chem. A* **7** 10739
[27] Scheer R and Schock H W 2011 *Chalcogenide Photovoltaics* (Wiley)
[28] Moulder J F and Chastain J 1992 *Handbook of x-ray Photoelectron Spectroscopy: A Reference Book of Standard Spectra for Identification and Interpretation of XPS Data* (Physical Electronics Division, Perkin-Elmer Corp)
[29] Luo P *et al* 2023 Electron transport layer engineering induced carrier dynamics optimization for efficient Cd-free Sb_2Se_3 thin-film solar cells *Small* **20** 2306516
[30] Zhou Y *et al* 2017 Buried homojunction in CdS/Sb_2Se_3 thin film photovoltaics generated by interfacial diffusion *Appl. Phys. Lett.* **111** 013901
[31] Sze S M and Ng K K 2007 *Physics of Semiconductor Devices (Wiley-interscience* (Wiley)
[32] Qiu W, Zhang C, Cheng S, Zheng Q, Yu X, Jia H and Wu B 2019 The crystal structure, electronic structure and photoelectric properties of a novel solar cells absorber material $Sb_2Se_{3-x}S_x$ *J. Solid State Chem.* **271** 339
[33] Sasaki K 1974 Study on work function of the {0001} faces of CdS crystal. I *Jpn. J. Appl. Phys.* **13** 933
[34] Zhu Y and Xiao Z 2025 Defect engineering in CdS: resolving p-type doping controversies and enabling breakthrough n-type conductivity for thin-film photovoltaics *J. Phys. Chem. Lett.* **16** 11144
[35] Fonash S F, Fraas L M, Hamakawa Y, Hill R, Kazmerski L L, Meakin J, Rothwarf A and Wagner S 1985 *Current Topic in Photovoltaics* ed T J Couts and J D Meakin (Academic)
[36] Ren D, Cathelinaud M, Ma H and Zhang X 2021 Carrier recombination and transport for Sb_2Se_3-based homojunction thin film solar cells *MRS Adv.* **6** 609
[37] Mavlonova A *et al* 2020 A review of Sb_2Se_3 photovoltaic absorber materials and thin-film solar cells *Sol. Energy* **201** 227